SOFT ROBOTICS
Volume 00, Number 00, 2020

DOI: 10.1089/soro.2020.0037

SoRo
Soft Robotics

Fluid Mechanics of Pneumatic Soft Robots

Peter Breitman,[1] Yoav Matia,[2] and Amir D. Gat[1]

Abstract

Pressurization of gas within embedded channels and cavities is a popular method for actuating soft robots. Various previous works examined the effects of internal fluid mechanics on this actuation approach, as well as on leveraging viscous effects to extend the capabilities of soft robots. However, no existing works studied the combined effects of fluid viscosity and compressibility, relevant to miniaturized configurations, which is the aim of the current work. We derive a general model for compressible viscous flow in an elastic media representing a simplified miniaturized soft robot. We illustrate applying this model to periodic configurations, simplifying it via a long-wave approximation. Steady, and time-dependent solutions are obtained, allowing to model the flow and to provide insight into the actuation dynamics of miniaturized pneumatic soft robots.

Keywords: actuation, viscous peeling, compressible flow, elastic beams, long-wave, approximation

Introduction

Pressurization of gas within elastic chambers is a popular method for the actuation of soft robots, resulting in stress at the gas–solid interface, and thus, a desired deformation of the structure. It is commonly assumed that the pressure within the internal cavities propagates sufficiently fast so that a uniform pressure exists throughout all gas in the structure. Although this assumption is justified for many configurations, miniaturization of the internal cavities, or the entire soft robot (which is desired for many applications[1,2]), increases viscous resistance and may create significant pressure variations as well as delays of actuation response. These significant pressure variations, appearing due to the large viscous resistance characterizing miniaturized configurations, yield sizeable density variations, commonly denoted as ''low Mach compressibility.'' These density variations, in turn, modify the flow-field within the soft robot,[3–5] and thus significantly affect its operation.

Viscous flow in contact with elastic structures, which is the subject of the current work, has been studied extensively in diverse fields of research and applications. These include flows in bio-medical systems (e.g., flow inside blood vessels[6] and the opening of airways[7,8]), geophysics,[9–12] impact mitigation,[13] and more.[14–18] Viscous flows within elastic structures are particularly of importance in the field of soft robotics, since configurations that include soft elastic channels, filled with pressurized fluid, are ubiquitous in this field. Various previous works examined the effects of incompressible viscous flow on soft actuators and soft robots. A partial list of these works include Chang *et al.*,[19] who conceived a low pressure bending fluid-driven actuator, achieving high moments and angular displacement over length, and later used the same principle to create a more versatile actuator, while achieving miniaturization.[20] Mazlouman *et al.*[21] created an antenna-like actuator, able to bend in all directions by using eccentric axial channels, filled with fluid. Matia and Gat[22] and Matia *et al.*[23] developed an analytical model for an embedded fluidic channel network, and they verified it experimentally. Zhakypov *et al.*[24] created a method of designing a fluid-driven, self-folding origami structures. Vasios *et al.*[25] created a discrete model for analyzing fluid-driven actuators with repeating patterns.

Other relevant works on gas-driven actuators include those by Shapiro *et al.*,[26] who created a single-degree-of-freedom, gas-actuated bending actuator, achieving large displacements. Milana *et al.*[1] developed a process of manufacturing micro-scale inflatable actuators. Zhang *et al.*[27] studied pneumatically driven actuators for three-dimensional (3D) printed origami skeletons, Hines *et al.*[28] studied an inflatable sealed-chamber soft robot actuator, controlled by a dielectric-elastomer actuator, which eliminates the need for the constant flow of gas. Although pressurization of gas within internal cavities is a very commonly used method in soft robotics

[1]Faculty of Mechanical Engineering, Technion, Israel Institute of Technology, Haifa, Israel.
[2]Sibley School of Mechanical and Aerospace Engineering, Cornell University, Ithaca, New York, USA.

([1,26–28] among many others), no existing works studied the combined effects of fluidic viscosity and compressibility, relevant to miniaturized configurations. Understanding such effects is of importance in designing gas-driven actuators, apart from understanding the challenges in the actuation of miniaturized soft robots. Hence, this work aims at deriving a general simplified model, which can be used to provide insight, as well as quantitative predictions regarding the fluid mechanics occurring within gas-driven miniaturized soft robots, and the resulting deformation of the structure.

This work is organized as follows: In A Simplified Model of a Flow within Miniaturized Pneumatic Soft-Robot section, we derive a general governing equation for compressible viscous flow in elastic channels. In Long-Wave Approximation for Configurations with Repeating Unit Cells section, we apply a long-wave approximation to model a common periodic actuator configuration involving multiple identical cells (as illustrated in Fig. 1).

In Analytic Solutions section, we present steady-state and transient solutions for actuation of a gas-driven soft-actuator, and in Concluding Remarks section, we provide concluding remarks.

A Simplified Model of a Flow within Miniaturized Pneumatic Soft Robots

We begin by deriving the equation governing the flow of a viscous compressible fluid within an elastic domain, representing a very simplified version of a gas-actuated soft robot. The configuration is illustrated in Figure 2. We denote the stream-wise direction by x_f, and the cross-sectional coordinate vector by $\boldsymbol{x_{cs}}$ (for axi-symmetric configuration $\boldsymbol{x_{cs}}$ is the radial direction r_f, as presented in Fig. 2). Implementing the lubrication assumptions of negligible inertial effects and geometrical slenderness, as well as an ideal gas model, it follows that the pressure, in leading order, does not vary in-plane $p = p(x_c, t)$ (for complete lubrication derivation see Leal[29]). The Navier–Stokes equations are, thus, simplified to the following equation of stream-wise momentum (for detailed justification using lubrication theory, see Appendix A1)

$$\nabla_{cs}^2 u = \frac{1}{\mu}\frac{\partial p}{\partial x_f}, \tag{1}$$

where x_f and $\boldsymbol{x_{cs}}$ are the stream-wise and the in-plane directions, respectively; u and $\boldsymbol{u_{cs}}$ are the stream-wise and the in-plane flow velocities, corresponding to the aforementioned directions, respectively; ∇_{cs} is the two-dimensional in-plane Nabla operator; p is the relative (gauge) pressure of the fluid; μ is viscosity; and ρ is the density of the fluid. The stream-wise momentum equation is supplemented by the equation of mass conservation

$$\frac{\partial \rho}{\partial t} + \frac{\partial}{\partial x_f}(\rho u) + \nabla_{cs} \cdot (\rho \boldsymbol{u_{cs}}) = 0, \tag{2}$$

and for compressibility modeling—the ideal gas state equation,

$$p + p_{atm} = \rho \mathcal{R} \tau_0, \tag{3}$$

where $\mathcal{R}, \tau_0$ are the specific ideal gas constant and temperature, respectively. Here, we assume that the gas temperature is equal everywhere to the solid temperature, due to sufficiently rapid heat transfer to the solid. Thus, temperature changes due to gas expansion are neglected, and temperature is determined by the solid. This fact sets $\mathcal{R}\tau_0$ to be a constant, and it allows us to replace ρ with $p + p_{atm}$ in Equation (2).

Equation (1) is the in-plane Poisson's equation with regards to the cross-section, described by coordinates $\boldsymbol{x_{cs}}$. For any cross-sectional shape, solving (Eq. 1) along with the homogeneous Dirichlet boundary conditions (no-slip condition at the boundaries) yields a solution of the form

$$u = \frac{1}{\mu}\frac{\partial p}{\partial x_f} f(\boldsymbol{x_{cs}}), \tag{4}$$

where $f(\boldsymbol{x_{cs}})$ is dependent on the geometry of the cross-section, and thus the total flux, obtained by integrating u across the cross-section a is given by

$$q = \int_a u \, d\boldsymbol{x_{cs}} = \frac{1}{\mu}\frac{\partial p}{\partial x_f} q_1, \tag{5}$$

where $q_1(x_f, p)$ is the integral permeability of the channel cross-section. Note that the pressure dependency of q_1 comes

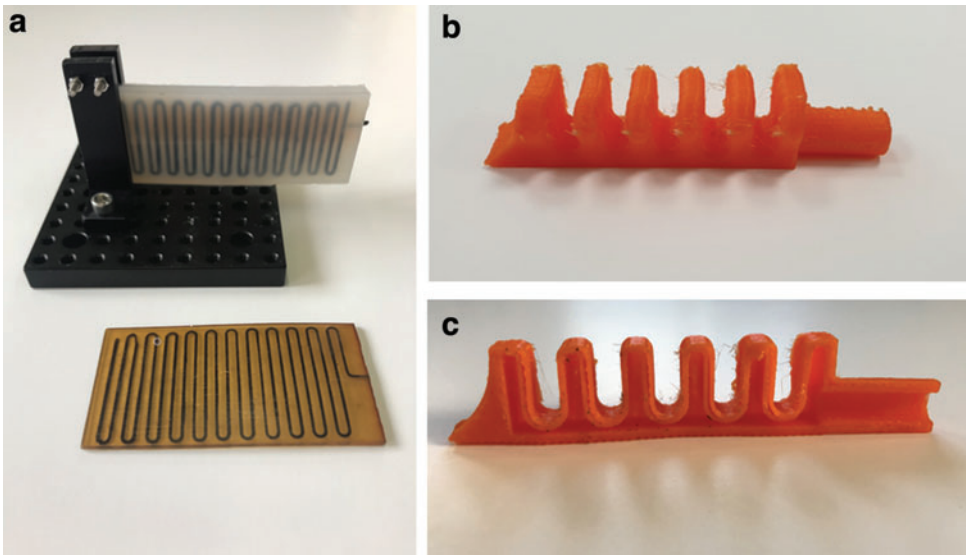

FIG. 1. Common gas-driven actuator configurations. **(a)** Beam with embedded network of serpentine channels, working as a bending actuator. **(b)** Cascaded bladders bending actuator, and **(c)** the internal channels and bladders. Color images are available online.

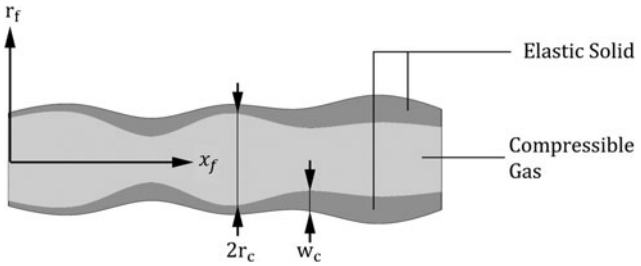

FIG. 2. An illustration of the simplified model problem. x_f represents the stream-wise coordinate of the channel, and r_f is the radial coordinate. r_c is the inner channel radius at rest, and w_c is the thickness of the solid tube.

from the elastic deformation of the cross-section area, which is pressure dependent, rather than directly from Equation (5).

Integrating (Eq. 2) over the cross-section area, we obtain

$$\int_a \frac{\partial}{\partial t}(p+p_{atm})\,d\boldsymbol{x_{cs}} + \int_a \frac{\partial}{\partial x_f}[(p+p_{atm})u]\,d\boldsymbol{x_{cs}} + \int_a \nabla_{\boldsymbol{cs}}\cdot[(p+p_{atm})\boldsymbol{u_{cs}}]\,d\boldsymbol{x_{cs}} = 0, \tag{6}$$

where $a(x_f,p)$ is the cross-section area. Implementing Reynolds transport theorem on the first two terms, and Gauss theorem on the third term yields

$$\int_a \frac{\partial}{\partial t}(p+p_{atm})\,d\boldsymbol{x_{cs}} = \frac{\partial}{\partial t}\int_a (p+p_{atm})\,d\boldsymbol{x_{cs}} - \oint_{\partial a}(\boldsymbol{u_{cs}}\cdot\boldsymbol{n})(p+p_{atm})\,ds, \tag{7}$$

$$\int_a \frac{\partial}{\partial x_f}[(p+p_{atm})u]\,d\boldsymbol{x_{cs}} = \frac{\partial}{\partial x_f}\int_a [(p+p_{atm})u]\,d\boldsymbol{x_{cs}} - \oint_{\partial a}(\boldsymbol{u_{cs}}\cdot\boldsymbol{n})(p+p_{atm})u\,ds, \tag{8}$$

$$\int_a \nabla_{\boldsymbol{cs}}\cdot[(p+p_{atm})\boldsymbol{u_{cs}}]\,d\boldsymbol{x_{cs}} = \oint_{\partial a}[(p+p_{atm})\boldsymbol{u_{cs}}\cdot\boldsymbol{n}]\,ds, \tag{9}$$

where ∂a is a contour, representing the boundary of the section, such that ds is a small section of it. Note that since $\boldsymbol{u_{cs}} = \boldsymbol{0}$ on the boundary due to no-penetration conditions, all boundary integrals vanish. In addition, since $p + p_{atm}$ is independent of $\boldsymbol{x_{cs}}$, it is constant with respect to all integrals. This yields

$$\frac{\partial}{\partial t}\left[(p+p_{atm})\int_a d\boldsymbol{x_{cs}}\right] + \frac{\partial}{\partial x_f}\left[(p+p_{atm})\int_a u\,d\boldsymbol{x_{cs}}\right] = 0, \tag{10}$$

and finally

$$\frac{\partial}{\partial t}[(p+p_{atm})a] + \frac{\partial}{\partial x_f}\left[(p+p_{atm})\frac{1}{\mu}\frac{\partial p}{\partial x_f}q_1\right] = 0, \tag{11}$$

Equation (11) is, in fact, a form of the Reynolds lubrication equation, with the cross-section area serving as the varying profile. It is a partial differential equation with regard to the fluidic pressure, and it is the governing equation for flow field and requires known functions of cross-section $a(x_f,p)$ and viscous resistance $q_1(x_f,p)$. To apply this equation in a specific system, both $a(x_f,p)$ and $q_1(x_f,p)$ need to be fitted to the properties of the soft robot. To further simplify the governing equation, we may examine an axi-symmetric configuration, as illustrated in Figure 2. Although this axi-symmetric model is a rough approximation of realistic configurations, it allows for spatial variation of the structural rigidity (hereby change to the tube thickness) and integral permeability (hereby change to the cross-section), thus allowing to capture the principal mechanisms governing the flow.

The deformation of the cross-section in this case is approximated to the thin cylindrical shell model,[17]

$$d = \frac{pr_c^2}{Ew_c}, \tag{12}$$

where $r_c(x_f)$ is the radius of the undeformed cross-section, E is Young's modulus, and $w_c(x_f)$ is the shell thickness. Hence, the area relation to pressure is

$$a = \pi\left(r_c + \frac{pr_c^2}{Ew_c}\right)^2. \tag{13}$$

For axi-symmetric configurations there is an immediate solution of Equation (1), yielding the standard Hagen–Poiseuille flow-field

$$u(x_f, r_f, t) = \frac{1}{4\mu}\frac{\partial p}{\partial x_f}\left(r_f^2 - r_c^2\right), \tag{14}$$

where r_f is the radial coordinate inside the cross-section. Note that the dependence on time t comes from the pressure gradient. Next, we integrate across the section to obtain the mass-flux q

$$q = 2\pi\int_0^{r_c+d} u(x_f,r_f)\,r_f\,dr_f = -\frac{\pi(r_c+d)^4}{8\mu}\frac{\partial p}{\partial x_f} = -\frac{1}{8\pi\mu}\frac{\partial p}{\partial x_f}a^2. \tag{15}$$

Thus, from Equations (5) and (15), $q_1(p,x_f)$ is

$$q_1 = -\frac{\pi}{8}\left(r_c + \frac{pr_c^2}{Ew_c}\right)^4. \tag{16}$$

Substituting $a(p)$ (Eq. 13) and q_1 (Eq. 16) into the governing evolution equation (11) yields

$$\frac{\partial}{\partial t}\left[(p+p_{atm})\pi r_c^2\left(1+\frac{pr_c}{Ew_c}\right)^2\right] = \frac{1}{8\pi\mu}\frac{\partial}{\partial x_f}\left[(p+p_{atm})\frac{\partial p}{\partial x_f}(\pi r_c^2)^2\left(1+\frac{pr_c}{Ew_c}\right)^4\right], \tag{17}$$

which is the governing equation for axi-symmetric configurations.

To complete the description of the dynamics of a soft robot, this model for the fluidic pressure needs to be combined with a model for the global deformation of the structure, and the values of the integral permeability and rigidity need to be fitted at each location to the specific configuration examined. This approach will be illustrated in the following sections.

Long-Wave Approximation for Configurations with Repeating Unit Cells

Many soft actuators comprise multiple similar fluid-filled chambers, forming a structure of repeating unit cells. This gives the system a discrete nature. The method of long-wave approximation is used to view discrete systems as continuous ones, by assuming the change between two adjacent unit cells is small (e.g., the ''wave,'' or any other phenomenon is stretched across multiple unit cells, i.e., long). In these configurations, it is possible to simplify the model further by implementing the long-wave approximation, and thus represent a spatially varying configuration by uniform averaged properties. A configuration consisting of such repeating unit cells is illustrated in Figure 3. The internal flow within this configuration is here approximated by an axisymmetric model (Eq. 17) with periodic changes in the channel radius, representing the transition between the chambers and the smaller connecting channels,

$$r_s(x_c) = r_1 + \sum_{i=1}^{N} (r_2 - r_1)\left[H\left(x - \frac{2i-1}{2N}\right) - H\left(x - \frac{i}{N}\right)\right], \tag{18}$$

where r_2 is the hydraulic radius of the bladders, r_1 is the hydraulic radius of the tubes connecting the bladders, N is the number of repeating cells, and $H(x-a)$ is the Heaviside function. To relate the fluidic pressure to the structural deformation, we assume here a simple linear relation

$$(\theta_n - \theta_{n-1}) = c\,(p - p_a)|_{x_c = x_b}, \tag{19}$$

where θ_n is the angular deformation created the n^{th} bladder, x_b is the location of the center of the bladder, and c is a compliance constant, which can be quantified by experiments or numerical calculations. Both relations (Eq. 18) and (Eq. 19) are chosen here for simplicity, without limitation of generality, and may be adapted and modified to any specific configuration.

As part of the long-wave approximation, we require that the pressure drop in each cell is small compared with the pressure drop across the entire configuration. For this reason, the validity of the approximation improves when there are multiple cells inside a given length of system. The long-wave form of the fluidic evolution of Equation (11) is

$$\frac{\partial}{\partial t}\left[(p + p_{atm})\bar{a}\right] + \frac{\partial}{\partial x_s}\left[(p + p_{atm})\frac{1}{\mu}\frac{\partial p}{\partial x_s}\bar{q}_1\right] = 0, \tag{20}$$

where $\bar{q}_1(p)$ and $\bar{a}(p)$ are the equivalent cross-section area and integral permeability in each periodic cell, respectively. Averaging over the area $a(p)$, and the viscous resistance $1/q_1(p)$ yields,

$$\bar{a}(p) = \frac{1}{l_{cell}}\int_0^{l_{cell}} a(p)\,d\xi \quad \text{and} \quad \bar{q}_1 = \left(\frac{1}{l_{cell}}\int_0^{l_{cell}} \frac{d\xi}{q_1}\right)^{-1}. \tag{21}$$

Substituting into (Eq. 21) relations (Eq. 13) and (Eq. 16), along with the periodic (Eq. 18), provides the averaged area

$$\bar{a}(p) = \pi\left(r_1 + \frac{pr_1^2}{Ew_1}\right)^2 \frac{l_1}{l_{cell}} + \pi\left(r_2 + \frac{pr_2^2}{Ew_2}\right)^2 \frac{l_2}{l_{cell}}. \tag{22}$$

and averaged permeability

$$\bar{q}_1 = -\frac{\pi}{8}\left(r_1 + \frac{pr_1^2}{Ew_1}\right)^4 \left(r_2 + \frac{pr_2^2}{Ew_2}\right)^4 \left[l_2\left(r_1 + \frac{pr_1^2}{Ew_1}\right)^4 + l_1\left(r_2 + \frac{pr_2^2}{Ew_2}\right)^4\right]^{-1}, \tag{23}$$

for the configuration illustrated in Figure 3.

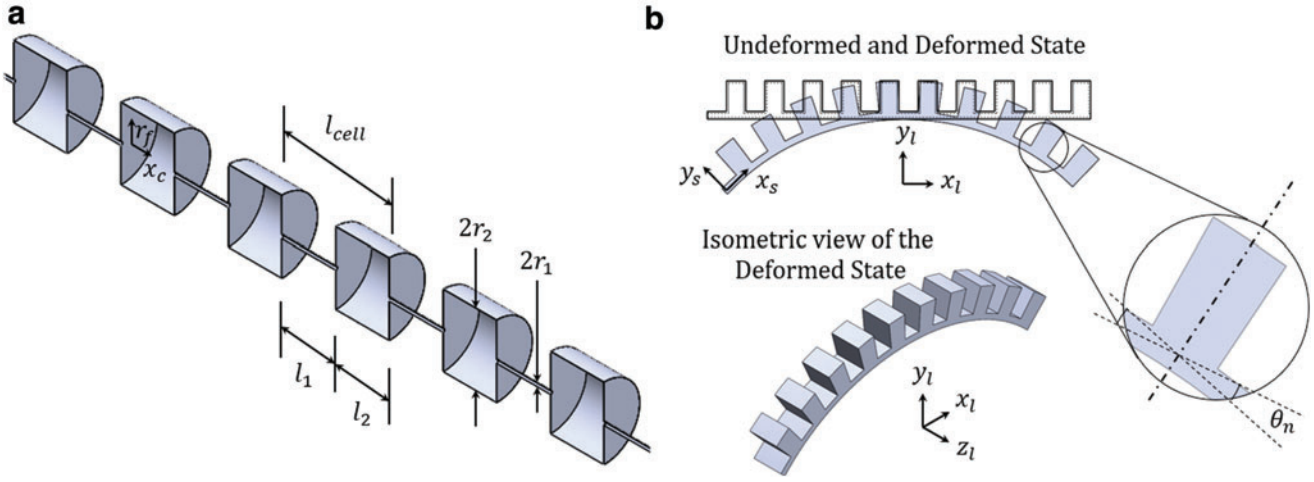

FIG. 3. A series of bladders connected by slender channels. **(a)** The fluidic channel model, approximating the internal channel by an equivalent axi-symmetric tube. **(b)** A bending actuator at rest and at a deformed state. Note that x_f, y_f are the fluidic coordinates; x_s, y_s are the actuator coordinates; and $x_|$, $y_|$, $z_|$ are the laboratory coordinates. Color images are available online.

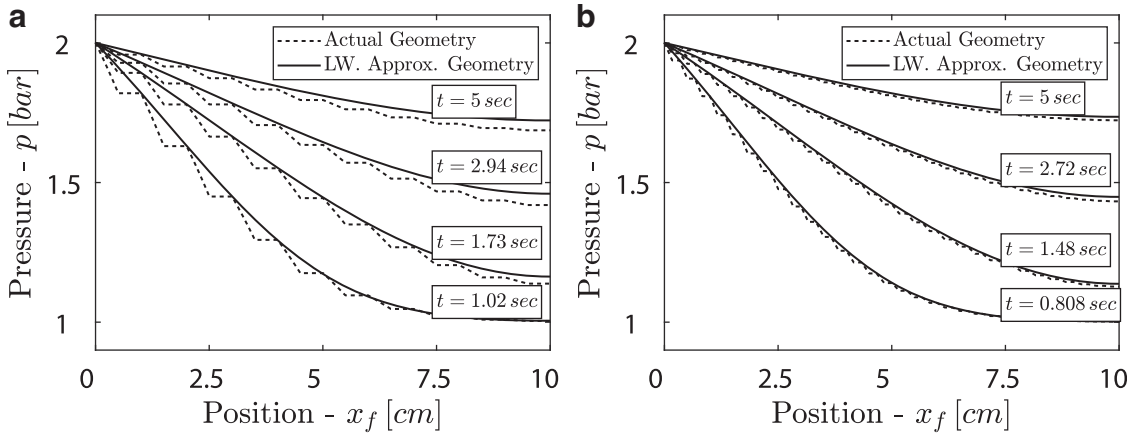

FIG. 4. The pressure profile (*dashed lines*) calculated from Equation (17), for different times and **(a)** 10 bladders or **(b)** 30 bladders. The *solid black lines* mark the LW approximation (Eq. 20) for each case. LW, long-wave.

Solving the governing equation for the gaseous pressure field (Eq. 11), or the simplified long-wave approximation version of Equation (20), we can now observe the actuation dynamics of a characteristic actuator, as well as examine the validity of the long-wave approximation. The parameters used for the presented computations are total channel length $l = 10cm$, number of bladders $N = 10$ or 30, connecting channel radius $r_1 = 50\mu m$, bladder radius $r_2 = 1mm$, uniform wall thickness of $w_1 = w_2 = 5\mu m$, fluid viscosity $\mu = 18.5 \cdot 10^{-6} Pa \cdot sec$, and material elasticity modulus of polydimethylsiloxane—$E = 10MPa$. Calculations are performed for the period of $T_f = 5\,sec$, where the pressure is suddenly increased at $t = 0$. The appropriate boundary and initial conditions are given by

$$p(x_c, t=0) = 10^5 Pa, \quad p(x_c = 0, t > 0) = 10^5 Pa + H(t)10^5 Pa, \quad \frac{\partial p}{\partial x}(x_f = l, t) = 0, \tag{24}$$

where the last condition in Equation (24) describes a closed end at $x_f = l$, blocking the flow.

Figure 4 shows the pressure fields for 10 and 30 bladders. Note that the solution of Equation (17) yields that the pressure is nearly uniform in the bladder segments, as was expected due to the small viscous resistance in these regions compared with the connecting channels. The different curves, which represent the pressure field in different times, converge in an exponentially decaying manner toward a steady state of spatially uniform pressure. As seen from Figure 4, the long-wave approximation yields a better result as the number of bladders increases, and it validates the long-wave approximation. The deformation, shown in Figure 5, was calculated by using a compliance coefficient value of $c = 3 \cdot 10^{-5} Pa^{-1}$, meaning that each bladder creates a relative angle of 3° per 1 Bar. A time scale of the order of 10 seconds is observed, and thus there is a significant delay in the actuation, where the bladders near the inlet are actuated first, and the pressure gradually propagates. This time scale depends on viscous effects, solid elasticity, and the gas compressibility. In the next section, we will examine the propagation dynamics in detail, and obtain the dimensional parameters governing this problem.

Analytic Solutions

Although numerical solutions of the fluidic evolution in Equation (20) are possible for specific cases (as shown in the

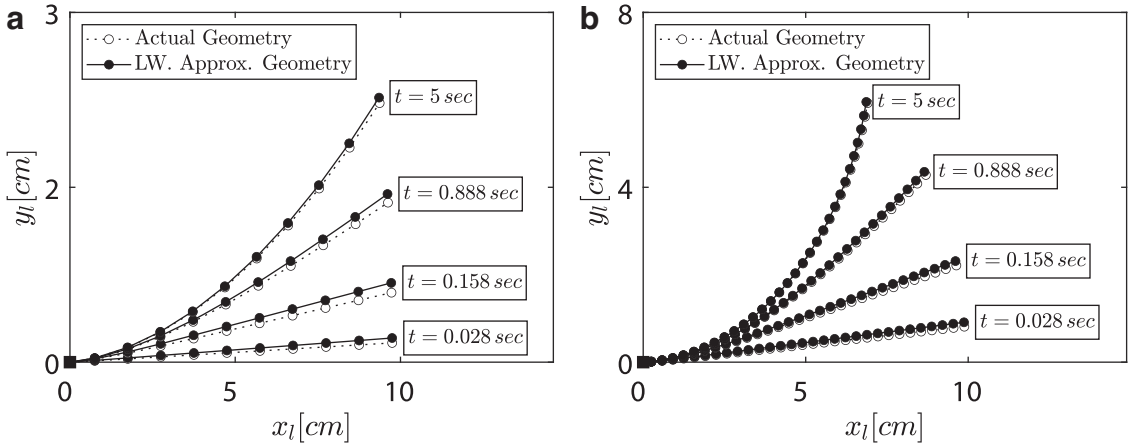

FIG. 5. The actuator deformation profiles, corresponding to the pressure calculated from Equation (17) for **(a)** 10 and **(b)** 30 bladders. *Dashed lines* mark numerical solutions of Equation (17), and *solid black lines* mark the LW approximation (Eq. 20).

previous section), more insight regarding the behavior of such systems in different limits may be obtained from analytical investigation. The long-wave approximation derived in the previous section allows us to relate the problem of gas flow within a periodic soft actuator to previous works on gas flow into uniform elastic micro-channels.[18,27] However, although the long-wave approximation yields a similar governing equation, it involves higher powers of the pressure variable p and we thus derive new steady-state and transient analytic solutions for the current system, using similar approach as in Elbaz et al.[18]

We will focus in this section on configurations where the averaged area $\bar{a}$ and integral permeability $\bar{q}_1$ are in the form

$$\bar{a} = \frac{l_1 + l_2}{l_{cell}} \pi \left(r_1 + \frac{p r_1^2}{E w_1} \right)^2, \quad \text{and} \quad \bar{q}_1 = -\frac{l_{cell}}{l_1 + l_2} \frac{\pi}{8} \left(r_2 + \frac{p r_2^2}{E w_2} \right)^4. \tag{25}$$

This occurs in the common configuration where the bladders are much larger than the connecting tubes, as is the case illustrated in Figure 2. In this case, the majority of fluidic volume is in the bladder region (marked by subscript 1) and the viscous resistance is mainly due to the connecting channels (marked by subscript 2). In addition, such a form is also obtained when the properties of the connecting channels and the bladders are identical, as illustrated in Figure 6. In that case, the average properties are

$$\bar{a} = \frac{l_1 + l_2}{l_{cell}} \pi \left(r_c + \frac{p r_c^2}{E w} \right)^2, \quad \text{and} \quad \bar{q}_1 = -\frac{l_{cell}}{l_1 + l_2} \frac{\pi}{8} \left(r_c + \frac{p r_c^2}{E w} \right)^4 \tag{26}$$

(we note here that $l_1 + l_2 = l_{cell}$ only if the stream-wise direction x_f is always identical to x, otherwise, $l_1 + l_2 > l_{cell}$).

Rewriting (Eq. 20) with the long-wave correction and rearranging, we obtain the governing equation

$$\frac{\partial}{\partial t}\left[(p + p_{atm})\bar{a}\right] + \frac{1}{\mu}\left(\frac{l_1 + l_2}{l_{cell}}\right)^2 \frac{\partial}{\partial x_s}\left[(p + p_{atm})\bar{q}_1 \frac{\partial p}{\partial x_s}\right] = 0. \tag{27}$$

We define the dimensionless coordinates and variables

$$X_s = \frac{x_s}{l_s} \qquad T = \frac{t}{t^*} \qquad T = \frac{p_{in}}{\mu \Pi_E^2}\left(\frac{r_c}{l_s}\right)^2 \left(\frac{l_1 + l_2}{l_{cell}}\right)^2 t \qquad P = \frac{p}{p_{in}}, \tag{28}$$

and scaling analysis yields the following dimensionless parameters, which determine the physical regime of the internal flow

$$\Pi_P = \frac{p_{atm}}{p_{in}} \qquad \Pi_E = \frac{E w_c}{p_{in} r_c}, \tag{29}$$

where p_{in} is the inlet pressure, Π_P represents compressible effects (the limit $\Pi_P \to \infty$ is the limit of incompressible flow), and Π_E represents scale elastic effects (the limit $\Pi_E \to \infty$ is the limit of rigid channel). These are the governing parameters for the problem, which dictate the behavior of the solution, as well as the prominent physical regime in the system.

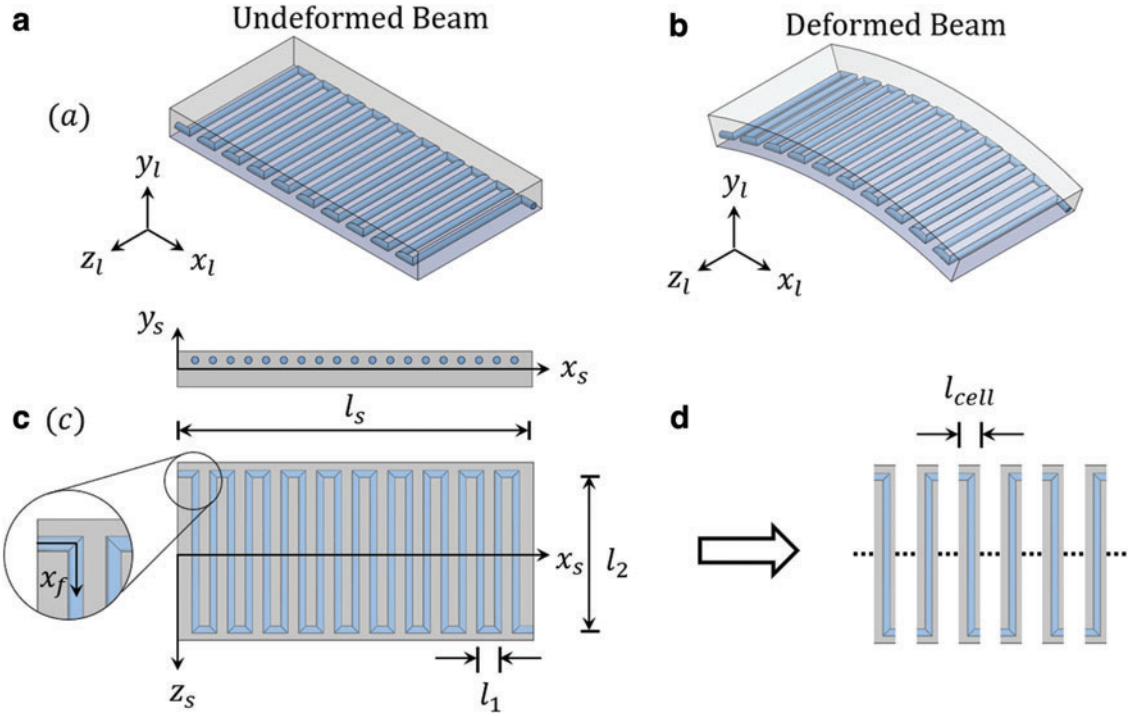

FIG. 6. Illustrations of a beam-shaped actuator with identical properties of the connecting tubes and bladders segments.[20,21] **(a, b)** Show the undeformed and deformed states of the beam, respectively. **(c)** Presents the internal structure of the serpentine channel, and its offset from the central axis of the beam to create asymmetry, which will be translated to a distributed load on the beam. z_s is the axial coordinate of the beam, I_s is the entire length of the beam, and I_{seg} is the length of one channel segment. **(d)** Illustrates the repeating segment used in the LW approximation. Color images are available online.

Substituting the dimensionless parameters into (Eq. 20) yields the dimensionless form of the governing equation

$$(P+\Pi_P)(3P+2\Pi_P+\Pi_E)\frac{\partial P}{\partial T} = \frac{1}{8}\frac{\partial}{\partial X_s}\left[(P+\Pi_P)(P+\Pi_E)^4\frac{\partial P}{\partial X_s}\right]. \quad (30)$$

In addition, to relate the gaseous pressure to the deformation of the beam, we choose here for simplicity a linear relation between the pressure and the angle created by the n^{th} bladder, $\theta_n = cp$, or in dimensionless form

$$\Theta_n = -P. \quad (31)$$

where $\Theta_n = \theta_n/\theta^*$ and $\theta^* = cp_{in}$.

Steady-state solutions

We first consider steady-state regimes, in which Equation (30) is reduced to

$$\frac{\partial}{\partial X_s}\left[(P+\Pi_P)(P+\Pi_E)^4\frac{\partial P}{\partial X_s}\right] = 0 \quad (32)$$

along with boundary conditions of $P(0)=1$ and $P(1)=0$. Thus, similar to the approach used in Elbaz et al.,[18] an implicit solution is readily available and given by the form

$$\left[6(1+\Pi_P)(1+\Pi_E)^5-(1+\Pi_E)^6-6\Pi_P\Pi_E^5+\Pi_E^6\right]X_s = 6(P+\Pi_P)(P+\Pi_E)^5-(P+\Pi_E)^6-6\Pi_P\Pi_E^5+\Pi_E^6. \quad (33)$$

By using Equations (33) and (31), the deflection profile of the beam is obtained. The case of incompressible flow can be obtained immediately from the current model by setting $\Pi_P \to \infty$. Figure 7 shows the beam deflection, corresponding to the pressure field, shown in the insets for both the compressible (dashed curve) and the incompressible cases (solid curve). For $\Pi_E, \Pi_P \gg 1$, we obtain a linear pressure distribution, as expected from incompressible viscous flow within a rigid channel. As seen in Figure 7, compressible fluid inside the channel creates larger deflections. This is true regardless of the compliance of the elastic domain, and Figure 7 presents this for three orders or magnitude of Π_E. Also, Figure 7 shows that for larger substrate compliance, there is greater variation in pressure gradient throughout the actuator, as most clearly evident in the region near the outlet $x \approx l$. However, this variation occurs in both the compressible and the incompressible case, leading to less difference between the compressible and the incompressible case as the solid is softer.

As part of our interest in implementing the presented model to actuation of soft robots, we would like to study the effects of compressibility and elasticity on the displacement of the tip of the actuator. To that end, we define the beam tip displacement as

$$D_{tip} = \int_0^1 \sin\Theta\, dX_s \quad (34)$$

where $\Theta(P)$ is a continuous function of angle change, obtained by performing long-wave approximation on the values of Θ_n. Next, we define ΔD_{tip} as the difference between D_{tip} by using compressible flow and D_{tip} by using incompressible flow under otherwise identical configuration. Figure 8 shows a parametric investigation of substrate stiffness Π_E and fluid compressibility Π_P, and their effect on ΔD_{tip}. Different curves in Figure 8a and b correspond to different values of Π_P and Π_E respectively. It is clearly seen in Figure 8b that larger values of Π_P lead to smaller difference in ΔD_{tip} for any value of Π_E, as the fluid gets compressed less and less, thus approaching the incompressible case. The same is observed in Figure 8a, as the curves approach zero as we increase Π_P. The effect of the stiffness of the substrate Π_E matches the behavior that was observed in Figure 7—the decrease in substrate stiffness decreases the deflection difference between the compressible and the incompressible case, as is evident from Figure 8a and b.

Validating our analytic model, a finite element model (FEM) 3D fluid-structure interaction model was set by using

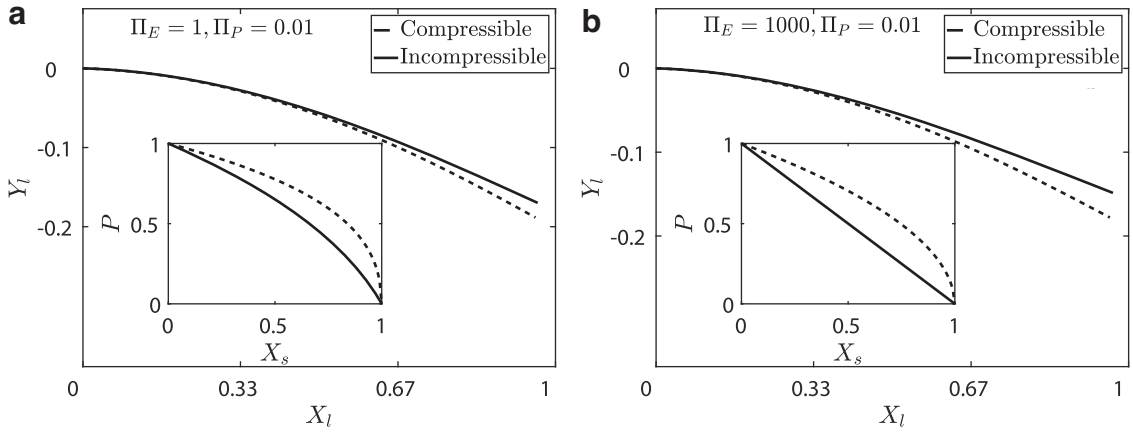

FIG. 7. A comparison of beam displacement for the case of gas (*dashed lines*) and an incompressible fluids (*solid lines*) for different pressures at the inlet and outlet sections, which create a steady internal flow. The displacement was calculated by using 25 equally spaced bladders ($I_{cells}/I_s = 1/25$). **(a)** Corresponds to (Π_E, Π_P) = (1,0.01), and **(b)** to (Π_E, Π_P) = (1000,0.01).

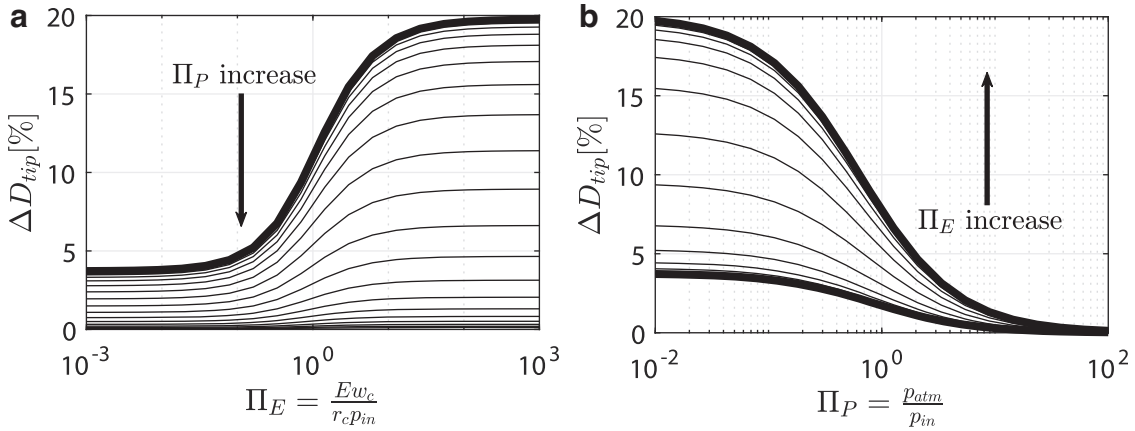

FIG. 8. The effects of the governing dimensional parameters Π_E **(a)** and Π_P **(b)** on ΔD_{tip}—the beam tip displacement difference between the compressible and incompressible cases, in percent. In **(a)**, each curve represents ΔD_{tip} versus Π_E for different values of Π_P. In this figure, lower curves represent larger values of Π_P. In **(b)**, each curve represents a different value of Π_E, where lower curves correspond to smaller values of Π_E.

COMSOL 5.2a commercial code. We enable geometric nonlinearity while limiting for a Hookean linear elastic material. The modeled system is a solid beam embedded with an internal serpentine channel array consisting of 18 channels set parallel to the z_s axis, and positioned above the neutral plane such that $r_c = w_c$, as illustrated in Figure 6. Beam physical parameters are $l_s = 1.4 \cdot 10^{-4} m$, $h_s = 1 \cdot 10^{-5} m$, $w_s = 5.4 \cdot 10^{-5} m$. The fluidic network channel has a square cross-section whose effective hydraulic radius is $r_c = 1 \cdot 10^{-6} m$ with $l_1 = 9.5 \cdot 10^{-6} m$ and $l_2 = 5 \cdot 10^{-5} m$. Beam material has a Young modulus of $E = 101 \cdot 10^6 Pa$, and the fluid is set as air. Gauge pressure boundary conditions are $p(x_s = 0) = 1.01 \cdot 10^6 Pa$ and $p(x_s = l_c) = 0 Pa$ with $p_{atm} = 1.01 \cdot 10^5 Pa$]. Substituting what has been stated earlier into (Eq. 29), the values for the system dimensionless parameters are $\Pi_P = 0.1$ and $\Pi_E = 100$. Fluid and solid domains' mesh consisted of $O(10^5)$ first- and second-order unstructured tetrahedral elements, respectively. An illustration of the FEM model is presented in Figure 9.

Figure 10a shows the comparison between the pressure solution obtained by the long-wave approximated model presented in this work, dimensionalized by the appropriate characteristic scales and the fully simulated FEM model. Great agreement is clearly seen for both compressible and incompressible flow. Figure 10b justifies the linear pressure-curvature relations given in Equation (19). Aside from the vicinity of the inlet (characterized by irregular local deformations that are neglected in the presented model), good agreement was observed between the actual pressure inside the channel, and the pressure, calculated by multiplying the curvature of the beam by c. Here, the value of $c = 5.1 \cdot 10^{-3} Pa/Rad$ was fitted. A better approximation is possible by adding terms of higher order to Equation (19), should the need arise.

Transient dynamics

Following Elbaz *et al.*,[18] we would like to gain insight on the problem, and specifically on the delay in actuation, by considering different limits of Π_P and Π_E and the governing Equation (30) for the case of a sudden increase in inlet pressure, as described later. In these cases, the governing Equation (30) is simplified to porous medium equations (PME), solved by Barenblatt[30]

$$\frac{\partial Q}{\partial T} = C \frac{\partial^2 Q^m}{\partial X_s^2}, \quad Q = P^n, \tag{35}$$

$$Q(0, T) = 1, \quad Q(1, T) = 0, \tag{36}$$

where C, m, n are constants, different for every limit. For the small deformation regime ($1 \ll \Pi_E, \Pi_P$), the values are: $C = \Pi_P \Pi_E^3 / 8(2\Pi_P + \Pi_E), m = n = 1$; for viscous-elastic

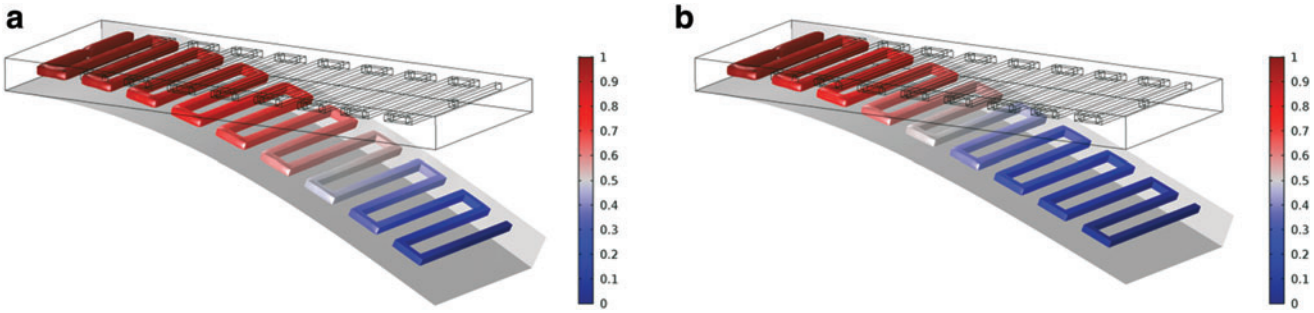

FIG. 9. FEM, illustrating a beam with a network of serpentine channels, as described in the Analytic Solutions section. Pressure distribution shown in legends is normalized $P = p/pin$. **(a)** Compressible flow. **(b)** Incompressible flow. The non-dimensional parameters of the system are $\Pi_P = 0.1$, $\Pi_E = 100$. FEM, finite element model. Color images are available online.

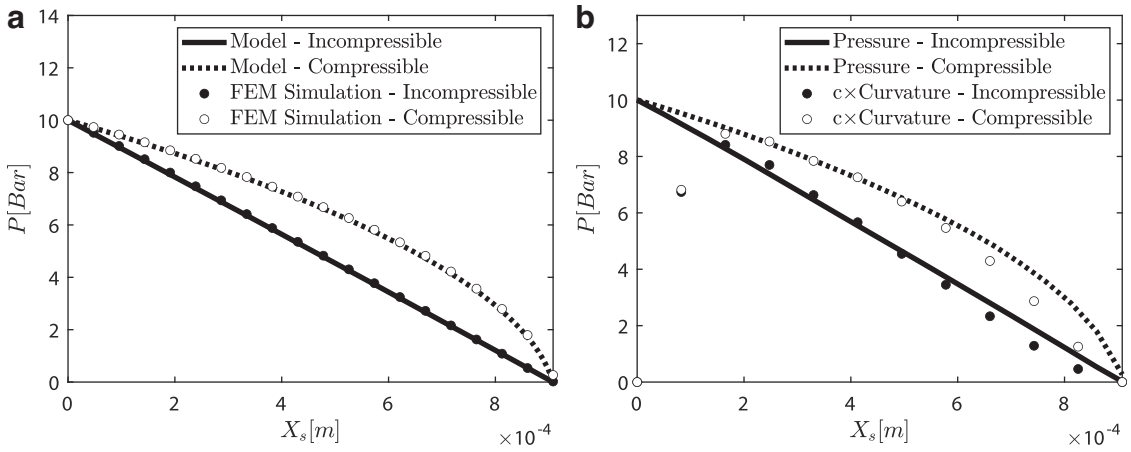

FIG. 10. **(a)** Shows a comparison between the pressure obtained from solving (Eq. 32) and implementing the proper characteristic quantities for dimensionalization (Eq. 28), and the pressure obtained from the FEM simulation. The *solid line* represents the pressure taken from the model for incompressible fluid and dashed for compressible, whereas the *black* and *white dots* represent the incompressible and compressible FEM model results, respectively. Good agreement is achieved in pressure distribution. Note the difference between the incompressible pressure field (which resembles Hagen–Poiseuille flow) and the compressible pressure field.

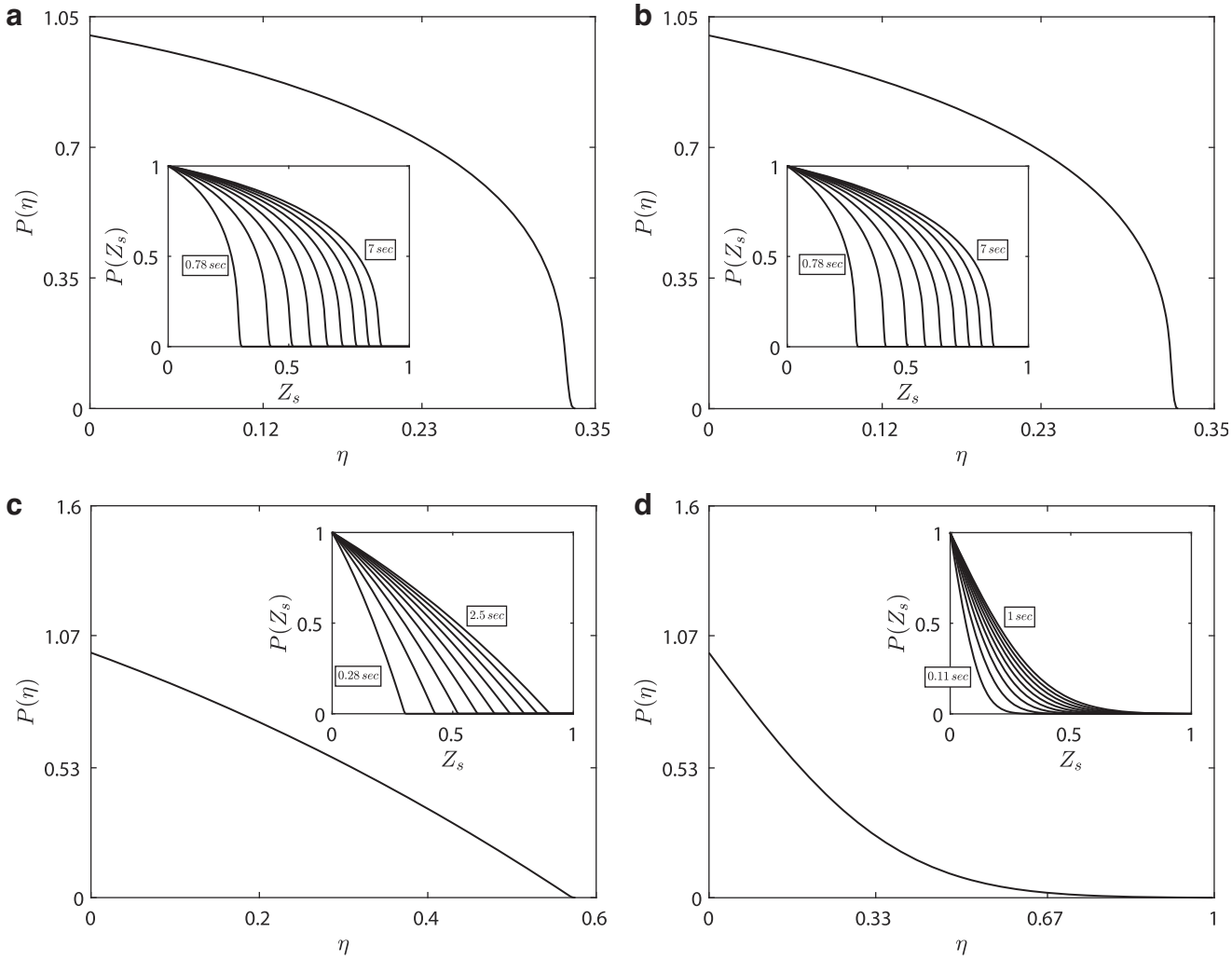

FIG. 11. Barenblatt self-similar solutions for pressure and deformation propagation for a sudden increase in inlet pressure, for the different regimes. Each panel represents a different regime: **(a)** for Π_P, $\Pi_E << 1$ (viscous-elastic-compressible regime), **(b)** for $\Pi_E << 1 << \Pi_P$, (viscous-elastic regime) **(c)** for $\Pi_P << 1 << \Pi_E$ (viscous-compressible regime) and **(d)** for $1 << \Pi_P$, Π_E (linearized limit). The *insets* present self-similar pressure profiles for different times.

regime ($\Pi_E \ll 1 \ll \Pi_P$), the values are: $C = 1/40, m = 2.5, n = 2$; for viscous-compressible regime ($\Pi_P \ll 1 \ll \Pi_E$), the values are: $C = \Pi_E^2/16, m = 2,\ n = 1$; and for compressible viscous-elastic regime ($\Pi_E, \Pi_P \ll 1$), the values are: $C = 1/48, m = 2, n = 3$.

For constant pressure at the inlet, a self-similar solution of Equations (35 and 36) for the different PME limits is available and valid until the front reaches the boundary of the channel. This equation is of the form

$$\eta = X_s T^{-1/2}, \quad Q(X_s, T) = f(\eta), \tag{37}$$

$$\frac{\partial^2 f^m}{\partial \eta^2} + \frac{\eta}{2C}\frac{\partial f}{\partial \eta} = 0, \tag{38}$$

$$f(0) = 1, \quad f(\eta \to \infty) = 0, \quad \frac{\partial f}{\partial \eta}(\eta \to \infty) = 0. \tag{39}$$

Apart from the small deformation limit ($\Pi_E \gg 1$ and $\Pi_P \gg 1$), in which the exact solution of Equations (38 and 39) is obtained analytically as an error function, the other cases require numerical calculation of the self-similar profile. These are presented in Figure 11, which shows the self-similar profiles, obtained by solving (Eqs. 38 and 39). These solutions, sometimes called the ''Barenlatt solutions,'' provide insight to the resulting deformation of the actuator. As seen in Figure 10, different relative scales of Π_E, Π_P, and P produce different regimes that are characterized by different shapes of the pressure profile. This is especially notable for the mainly compressible regime ($\Pi_P \ll 1 \ll \Pi_E$), and the small deformation limit ($1 \ll , \Pi_P, \Pi_E$). The location of the pressure front, X_{front}, is easily obtained from Equation (37) to be

$$X_{front} = \eta_f T^{1/2} \quad \rightarrow \quad x_{front} = \sqrt{\frac{p_{in}}{\mu}}\left(\frac{\eta_f}{\Pi_E}\right)\left(\frac{r_c}{l_s}\right)\left(\frac{l_1 + l_2}{l_{cell}}\right)t^{1/2}, \tag{40}$$

where η_f is different for the different regimes: $\eta_f \approx 0.34$ for $\Pi_P, \Pi_E \ll 1$, $\eta_f \approx 0.32$ for $\Pi_E \ll 1 \ll \Pi_P$, $\eta_f \approx 0.58$ for $\Pi_P \ll 1 \ll \Pi_E$, and $\eta_f \approx 0.99$ for $1 \ll \Pi_P, \Pi_E$. Although in all of the different regimes the time dependence of the pressure propagation remains the same, (i.e., $x_{front} \propto t^{1/2}$), the delay in actuation may vary significantly depending on the pressure and physical and geometric parameters of the actuator, which determine the physical regime in which it operates. Equation (40), thus, provides an estimate to the time scale in actuation delay, and the self-similar profiles describe the transient dynamics of the actuation.

Concluding Remarks

In this work, we derived a simplistic model for gas flow within an elastic tube with slowly varying properties. This model can be adapted to approximate various realistic actuator configurations, via fitting functions for area and viscous resistance. A long-wave approximation was used to simplify this governing equation for the case of configurations with repeating cells, which are common in the field of soft robotics. Finally, steady-state and transient (self-similar) analysis was performed to provide insight regarding the actuation dynamics. Four different regimes are obtained, and the time of actuation is estimated in each of the different regimes, as well as the transient pressure profile. The presented results provide a foundation for modeling the fluid mechanics within gas-actuated soft robots, as well as insight regarding the combined effects of viscosity, elasticity, and compressibility, on the actuation miniaturized pneumatic soft robots.

Author Disclosure Statement

No competing financial interests exist.

Funding Information

The authors thank the Israel Science Foundation (Grant No. 1285/20) for their contribution in funding this research.

References

1. Milana E, Belloti M, Gorissen B, *et al*. Precise bonding-free micromoulding of miniaturized elastic inflatable actuators. In: 2019 2nd IEEE International Conference on Soft Robotics (RoboSoft) COEX, Seoul, Korea, April 14–18, 2019. IEEE.
2. Zhang YF, Ng CJ, Chen Z, *et al*. Miniature pneumatic actuators for soft robots by highresolution multimaterial 3D printing. Adv Mater Technol 2019;4:1900427.
3. Gat A, Frankel I, Weihs D. Gas flows through constricted shallow micro-channels. J Fluid Mech 2008;602:427–442.
4. Shajii A, Freidberg JP. Theory of low Mach number compressible flow in a channel. J Fluid Mech 1996;313:131–145.
5. Punčochářová-Pořízková P, Kozel K, Horáček J, *et al*. Numerical simulation of unsteady compressible low Mach number flow in a channel. Eng Mech 2010;17:83–97.
6. Čanić S, Tambača J, Guidoboni G, *et al*. Modeling viscoelastic behavior of arterial walls and their interaction with pulsatile blood flow. SIAM J Appl Math 2006;67:164–193.
7. Grotberg JB, Jensen OE. Biofluid mechanics in flexible tubes. Annu Rev Fluid Mech 2004;36:121–147.
8. Jensen OE, Horsburgh MK, Halpern D, *et al*. The steady propagation of a bubble in a flexible-walled channel: asymptotic and computational models. Phys Fluids 2002;14:443–457.
9. Ball TV, Neufeld JA. Static and dynamic fluid-driven fracturing of adhered elastica. Phys Rev Fluids 2018;3:074101.
10. Medvedev S. Mechanics of viscous wedges: modeling by analytical and numerical approaches. J Geophys Res Solid Earth 2002;107:ETG-9.
11. Michaut C. Dynamics of magmatic intrusions in the upper crust: theory and applications to laccoliths on Earth and the Moon. J Geophys Res Solid Earth 2011;116:B05205.
12. Lister JR, Peng GG, Neufeld JA. Viscous control of peeling an elastic sheet by bending and pulling. Phys Rev Lett 2013;111:154501.
13. Tulchinsky A, Gat AD. Transient dynamics of an elastic Hele-Shaw cell due to external forces with application to impact mitigation. J Fluid Mech 2016;800:517–530.
14. Pihler-Puzović D, Juel A, Heil M. The interaction between viscous fingering and wrinkling in elastic-walled Hele-Shaw cells. Phys Fluids 2014;26:022102.
15. White JP, Heil M. Three-dimensional instabilities of liquid-lined elastic tubes: a thin-film fluid-structure interaction model. Phys Fluids 2005;17:031506.
16. Elbaz SB, Gat AD. Dynamics of viscous liquid within a closed elastic cylinder subject to external forces with application to soft robotics. J Fluid Mech 2014;758:221–237.

17. Elbaz SB, Gat AD. Axial creeping flow in the gap between a rigid cylinder and a concentric elastic tube. J Fluid Mech 2016;806:580–602.
18. Elbaz SB, Jacob H, Gat AD. Transient gas flow in elastic microchannels. J Fluid Mech 2018;846:460–481.
19. Chang BC, Berring J, Venkataram M, *et al*. Bending fluidic actuator for smart structures. Smart Mater Struct 2011;20: 035012.
20. Chang B, Chew A, Naghshineh N, *et al*. A spatial bending fluidic actuator: fabrication and quasi-static characteristics. Smart Mater Struct 2012;21:045008.
21. Mazlouman SJ, Chang BC, Mahanfar A, *et al*. Beam-steering antenna using bending fluidic actuators. IEEE Trans Antennas Propag 2013;61:5287–5290.
22. Matia Y, Gat AD. Dynamics of elastic beams with embedded fluid-filled parallel-channel networks. Soft Robot 2015;2:42–47.
23. Matia Y, Elimelech T, Gat AD. Leveraging internal viscous flow to extend the capabilities of beam-shaped soft robotic actuators. Soft Robot 2017;4:126–134.
24. Zhakypov Z, Mete M, Fiorentino J, *et al*. Programmable fluidic networks design for robotic origami sequential self-folding. In: 2019 2nd IEEE International Conference on Soft Robotics (RoboSoft), Seoul, Korea, April 14, 2019, pp. 814–820. IEEE.
25. Vasios N, Gross AJ, Soifer S, *et al*. Harnessing viscous flow to simplify the actuation of fluidic soft robots. Soft Robot 2020;7:1–9.
26. Shapiro Y, Wolf A, Gabor K. Bi-bellows: pneumatic bending actuator. Sens Actuator A Phys 2011;167:484–494.
27. Zhang M, Feng K, Zhang K, *et al*. Transient characteristics of a straight tube actuated by viscous compressible flow with consideration of large axisymmetric deformation. Acta Mechanica 2019;230:105–120.
28. Hines L, Petersen K, Sitti M. Inflated soft actuators with reversible stable deformations. Adv Mater 2016;28:3690–3696.
29. Leal LG. Advanced Transport Phenomena: Fluid Mechanics and Convective Transport Processes. Cambridge, UK: Cambridge University Press, 2007.
30. Barenblatt GI. On some unsteady motions of a fluid and a gas in a porous medium. Prikl Mat Makh 1952;16: 67–78.

Address correspondence to:
Peter Breitman
Faculty of Mechanical Engineering
Technion, Israel Institute of Technology
Technion City, Haifa 3200003
Israel

E-mail: petya@campus.technion.ac.il

Appendix A1

Appendix A1 Detailed Derivation of the Flow Model

In this appendix, we justify our choice of Equations (1 and 2) as the starting point of the analysis. Consider a flow of a compressible fluid (i.e., gas) inside a long tube. The general governing equation for the fluid is given by the stream-wise (Eq. A1) and in-plane (Eq. A2) momentum balance equations (Navier–Stokes), and the continuity Equation (A3)

$$\rho\left(\frac{\partial u}{\partial t}+\boldsymbol{u_{cs}}\cdot\nabla_{\boldsymbol{cs}}u+u\frac{\partial u}{\partial x_f}\right)=\mu\left(\nabla^2_{\boldsymbol{cs}}u+\frac{\partial^2 u}{\partial x_f^2}\right)-\frac{\partial p}{\partial x_f}\,, \tag{A1}$$

$$\rho\left(\frac{\partial \boldsymbol{u_{cs}}}{\partial t}+\boldsymbol{u_{cs}}\cdot\nabla_{\boldsymbol{cs}}\boldsymbol{u_{cs}}+u\frac{\partial \boldsymbol{u_{cs}}}{\partial x_f}\right)=\mu\left(\nabla^2_{\boldsymbol{cs}}\boldsymbol{u_{cs}}+\frac{\partial^2 \boldsymbol{u_{cs}}}{\partial x_f^2}\right)-\nabla_{\boldsymbol{cs}}p\,, \tag{A2}$$

$$\frac{\partial\rho}{\partial t}+\nabla_{\boldsymbol{cs}}\cdot(\rho\boldsymbol{u_{cs}})+\frac{\partial}{\partial x_f}(\rho u)=0\,, \tag{A3}$$

where ρ is the density of the fluid; u is the stream-wise velocity of the fluid; $\boldsymbol{u_{cs}}$ is the in-plane fluid velocity vector inside a cross-section located at x_f, which is the stream-wise coordinate of the system; $\nabla_{\boldsymbol{cs}}$ is the in-plane Nabla operator, determined explicitly by choosing the appropriate in-plane coordinate system; and p is the relative (''gauge'') pressure of the fluid.

To simplify the analysis, we perform an evaluation of characteristic quantities by normalization. To do so we define the following quantities:

$$\begin{aligned}&\rho=\rho^*\Lambda,\quad u=u^*U,\quad \boldsymbol{u_{cs}}=u^*_{\boldsymbol{cs}}\boldsymbol{U_{cs}},\quad p=p^*P,\\ &x_f=x_f^*X_f,\quad \boldsymbol{x_{cs}}=x^*_{\boldsymbol{cs}}\boldsymbol{X_{cs}},\quad t=t^*T\,.\end{aligned} \tag{A4}$$

Here, all small letters represent dimensional variables, capital letters represent normalized dimensionless variables, and asterisk superscript represents characteristic quantities. For the coordinates and the velocities, subscript f (for fluid) represents the stream-wise direction, whereas subscript cs (for cross-section) represents the in-plane directions. Substituting the normalized variables into the equations, as well as setting $u^*=x^*/t^*$ and rearranging yields

$$\begin{aligned}&\left(\frac{x^*_{cs}}{x^*}\right)\left(\frac{\rho^*u^*x^*}{\mu^*}\right)\Lambda\left[\frac{\partial U}{\partial T}+\left(\frac{u^*_{cs}}{u^*}\right)\boldsymbol{U_{cs}}\cdot\nabla_{\boldsymbol{cs}}U+\left(\frac{x^*_{cs}}{x^*}\right)U\frac{\partial U}{\partial X_f}\right]\\ &\quad=\nabla^2_{\boldsymbol{cs}}U+\left(\frac{x^*_{cs}}{x^*}\right)^2\frac{\partial^2 U}{\partial X_f^2}-\frac{p^*x^*_{cs}}{\mu u^*}\left(\frac{x^*_{cs}}{x^*}\right)\frac{\partial P}{\partial X_f}\,,\end{aligned} \tag{A5}$$

(Appendix continues →)

$$\left(\frac{u^*_{cs}}{u^*}\right)\left(\frac{x^*_{cs}}{x^*}\right)^2\left(\frac{\rho^* u^* x^*}{\mu^*}\right)$$
$$\Lambda\left[\left(\frac{x^*_{cs}}{x^*}\right)\frac{\partial \mathbf{U_{cs}}}{\partial T}+\left(\frac{u^*_{cs}}{u^*}\right)\boldsymbol{U_{cs}}\cdot\nabla_{\boldsymbol{cs}}\boldsymbol{U_{cs}}+\left(\frac{x^*_{cs}}{x^*}\right)U\frac{\partial \boldsymbol{U_{cs}}}{\partial X_f}\right]$$
$$=\left(\frac{u^*_{cs}}{u^*}\right)\left(\frac{x^*_{cs}}{x^*}\right)\nabla^2_{\boldsymbol{cs}}\boldsymbol{U_{cs}}+\left(\frac{u^*_{cs}}{u^*}\right)\left(\frac{x^*_{cs}}{x^*}\right)^3\frac{\partial^2 U}{\partial X_f^2}-\frac{p^* x^*_{cs}}{\mu u^*}\nabla_{\boldsymbol{cs}}P, \tag{A6}$$

$$\left(\frac{x^*_{cs}}{x^*}\right)\frac{\partial \Lambda}{\partial T}+\left(\frac{u^*_{cs}}{u^*}\right)\nabla_{\boldsymbol{cs}}\cdot(\Lambda\boldsymbol{U_{cs}})+\left(\frac{x^*_{cs}}{x^*}\right)\frac{\partial}{\partial X_f}(\Lambda U)=0. \tag{A7}$$

Next, defining the following dimensionless numbers

$$\varepsilon_1=\frac{u^*_{cs}}{u^*},\quad \varepsilon_2=\frac{x^*_{cs}}{x^*}\quad \mathrm{Re}=\frac{\rho^* u^* x^*}{\mu^*}, \tag{A8}$$

and rewriting (Eqs. A5–S7) we obtain

$$\frac{\partial P}{\partial X}=\nabla^2_{\boldsymbol{cs}}U+O(\varepsilon_2\mathrm{Re},\varepsilon_2^2\mathrm{Re},\varepsilon_1\varepsilon_2\mathrm{Re},\varepsilon_2^2), \tag{A9}$$

$$\nabla_{\boldsymbol{cs}}P=O(\varepsilon_1\varepsilon_2^3\mathrm{Re},\varepsilon_1^2\varepsilon_2^2\mathrm{Re},\varepsilon_1\varepsilon_2,\varepsilon_1\varepsilon_2^2), \tag{A10}$$

$$\varepsilon_2\frac{\partial \Lambda}{\partial T}+\varepsilon_1\nabla_{\boldsymbol{cs}}\cdot(\Lambda\boldsymbol{U_{cs}})+\varepsilon_2\frac{\partial}{\partial X_f}(\Lambda U)=0. \tag{A11}$$

Our flow geometry (a slender tube) dictates $\varepsilon_1,\varepsilon_2\ll 1$, as per the lubrication assumption. In addition, since we are considering a viscous flow, we set $\mathrm{Re}\ll 1$. This simplifies (Eqs. A9–A11) greatly, and it implies that the dimensional governing equations for the problem are given by:

$$\nabla^2_{\boldsymbol{cs}}u=\frac{1}{\mu}\frac{\partial p}{\partial x_f}, \tag{A12}$$

$$\frac{\partial \rho}{\partial t}+\nabla_{\boldsymbol{cs}}\cdot(\rho\boldsymbol{u_{cs}})+\frac{\partial}{\partial x_f}(\rho u)=0. \tag{A13}$$

This result is, in fact, the starting point of the analysis in A Simplified Model of a Flow within Miniaturized Pneumatic Soft-Robot section.